RESEARCH ARTICLE

Experimental study on wake flows of a live fish with time-resolved tomographic PIV and pressure reconstruction

Han Tu[1] · FuJun Wang[1] · HongPing Wang[2,3] · Qi Gao[1] · RunJie Wei[4]

Abstract

Volumetric measurement for the wake structures generated by a freely swimming zebra fish has been conducted by tomographic particle image velocimetry. The 3D flow visualization is recorded by four high speed cameras. The time-resolved three-dimensional flow structures are obtained and studied. λ_{ci}-criterion is applied to identify vortices induced by zebra fish locomotion, which clearly exhibits the instantaneous structures of three-dimensional vortex rings. Vortex rings are linked at angles and gradually lose coherence as they convect downstream. By investigating the distribution of momentum components and acceleration terms of the Navier-Stokes equations, it is found that vortex rings in the wake have an accelerating effect on the flow. And alternating orientations of vortex rings can result in a change of thrust direction between successive tailbeats. A pressure reconstruction technique is applied, revealing low pressure regions around vortex rings and relatively large pressure gradient at the connecting part of the linked vortex rings. Combined with the kinematic information of the flow field, the dynamic analysis introduced by the acceleration and pressure fields further strengthens the understanding of fish's propulsion mechanism.

1 Introduction

Through millions of years of evolution and natural selection, fish and many aquatic species have developed the capability to generate fast movements with low energy costs (Lighthill 1969). In addition, they are able to continuously react to the surrounding flow to maintain stability and their locomotion state (Flammang et al. 2011a). Compared with conventionally used man-made propulsors, fish exhibit a different paradigm of locomotion (Triantafyllou et al. 2000). By bending their bodies and oscillating multiple flexible fins, fish generate highly complicated three-dimensional vortices to obtain necessary thrust and momentum. Vortex

motions are described as the sinews and muscles of fluid motions (Küchemann 1965), and vortices created by fish are considered as "footprints" that reflect the momentum transfer from fish to water (Ting and Yang 2009). Therefore, it is significant to study and understand the vortex structures in the wake for the investigation of bio-inspired swimming mechanism and the design of biomimetic underwater vehicles.

In general, most fish species generate thrust by bending their bodies and extending the induced propulsive wave to their caudal fins (Sfakiotakis et al. 1999). Therefore, the propulsion pattern of the majority of fishes is body and/or caudal fin (BCF, classified by Motion Sfakiotakis et al. 1999) locomotion (Borazjani and Sotiropoulos 2008). According to Breder (2015), further modes of BCF locomotion could be identified, for example, *carangiform* mode and *thunniform* mode. These modes should be regarded as pronounced points within a continuum, and fish may exhibit multiple modes under different conditions (Sfakiotakis et al. 1999). It is necessary to mention that for *carangiform* and *thunniform* swimmers, their body undulations are further confined close to the tail, and thrust is provided by a stiff caudal fin (Sfakiotakis et al. 1999). Only understanding the motions of the fins does not explain how fish move (Flammang et al. 2011a), one needs to investigate the wake structures generated by

✉ Qi Gao
qigao@zju.edu.cn

1 State Key Laboratory of Fluid Power and Mechatronic Systems, School of Aeronautics and Astronautics, Zhejiang University, Hangzhou 310027, China

2 State Key Laboratory of Nonlinear Mechanics, Institute of Mechanics, Chinese Academy of Sciences, Beijing 100190, China

3 School of Engineering Sciences, University of the Chinese Academy of Sciences, Beijing 100049, China

4 MicroVec., Inc, Beijing 100083, China

fish locomotion. Wake generated by a BCF swimmer is the focused topic discussed in this study.

Many previous research works such as biomimetic experimental simulation and live fish experiment have been conducted to observe vortex patterns in the wake and investigate the correlation between the aquatic motion and the nearby flow structures. The biomimetic experimental simulation could be simplified as studying a pitching airfoil or panel, since the lateral motion is concentrated in the posterior portion of the body (Brooks and Green 2019). Green et al. (2011), Imamura and Matsuuchi (2013) and King et al. (2018) launched stereo particle image velocimetry (sPIV) experiments and used periodic pitching panels to mimic the caudal fin motion and studied the wake structures. The investigations of pitching panels significantly reveal the three-dimensional structures of the complex wakes generated by the bio-inspired propulsors. Characteristics of live fish kinematics may be neglected by investigating pitching panels, when the flow field is not equivalent to that being induced by a whole fish. As pointed out by Wolfgang et al. (1999a, 1999b), nearby flow structures are significantly affected by body kinematics; therefore, studying the wake structures generated by a live fish, or a fish-like robot, is important for the understanding of aquatic species locomotion. The experimental or numerical studies with a full fish model could be found in Zhu and Yue (2002), Mignano et al. (2019) and Brooks and Green (2019).

As for the investigations of live fish swimming and other behaviors, previous studies have researched the morphological development of live fish for different maneuvers, such as cruise swimming (Mwaffo et al. 2017), escape responses (Hale 2002; Danos and Lauder 2007; Witt et al. 2015) and predator-prey interaction (Adhikari and Longmire 2013), and conducted quantitative measurements of the flow fields around the tested creatures. Sfakiotakis et al. (1999) concluded that the wake behind the cruise swimmers consists of a staggered array of vortices of alternating rotation directions. Many two-dimensional experimental investigations revealed significant flow structures of swimming in relevant cross sections (Drucker and Lauder 2002; Sakakibara et al. 2004; Tytell and Lauder 2008; Ting and Yang 2009; Mwaffo et al. 2017; Shih et al. 2017), e.g., vortices and thrust jets induced by motions of fins. With the development of particle image velocimetry measurement, three-dimensional PIV studies have been carried out on the fish wakes. Flammang et al. (2011a) used volumetric 3-component velocimetry (V3V) to capture the three-dimensional wakes of a bluegill sunfish and a cichlid fish. Flammang et al. (2011b) used V3V to investigate the dual-ring vortex wake structure generated by a shark tail. Mendelson and Techet (2015) used three-dimensional synthetic aperture particle image velocimetry (SAPIV) to investigate the wake behind a freely swimming giant danio. Mendelson and Techet (2017, 2020) used SAPIV to study the wake generated by a jumping

fish. Because it inherently includes the effects of body kinematics and tail stiffness, live fish experiment could provide conclusive insights into fish swimming mechanism.

The development of tomographic particle image velocimetry measurement (Elsinga et al. 2006) also offers an approach of acquiring time-resolved three-dimensional data. As a mature technique on measuring volumetric flow fields, TPIV has been applied to investigations of many complicated flows (Scarano 2012; Gao et al. 2013), such as 3D wake behind a wall-mounted short cylinder (Zhu et al. 2017) and near-wall turbulence boundary layers (Wang et al. 2019). As for the live fish investigation using TPIV, Adhikari and Longmire (2013) studied the three-dimensional flow structures around the fish mouth and the prey and revealed different strategies of capturing the prey. Gemmell et al. (2014) showed that the fish can reduce its hydrodynamic signals when approaching to evasive prey. It is also worth noting that TPIV has been successfully applied to many other aquatic organisms, such as copepod (Murphy et al. 2012; Adhikari et al. 2015a), sea butterfly (Murphy et al. 2016), Antarctic krill (Murphy et al. 2013), Antarctic pteropod (Adhikari et al. 2015b, 2016; Mohaghar et al. 2019), Daphnia (Michaelis 2014; Skipper et al. 2019). The TPIV experimental method is certainly feasible on fish swimming observations. Furthermore, the time-resolved PIV data allow us to reconstruct the corresponding pressure field. By integrating the pressure gradient obtained from a material acceleration, or solving the Poisson equation, the pressure can be reconstructed. This technique has been widely applied in many scenarios (Fujisawa et al. 2005; Kat et al. 2010; Oudheusden 2013; Huhn et al. 2016; Wang et al. 2018).

In the current work, TPIV measurement is applied to investigate a freely swimming fish in a water channel. Meanwhile, a pressure reconstruction technique, which is based on the dynamic constraints imposed by the Navier-Stokes equations, is adopted. By collecting time-resolved three-dimensional wake structures, this study is aimed at importing acceleration and pressure fields into the analysis of characteristics of wake vortices from both kinematic and dynamic aspects, and inferring the effects of the vortex pattern on the thrusting, which can strengthen the understanding of fish propulsion mechanism. As an experimental reference, the results may support parallel efforts on the computational modeling/simulation of fish swimming and corresponding wakes and contribute to future underwater vehicle designs.

2 Experimental apparatus

2.1 Fish

Zebra fish (*Danio rerio*) were selected for this study since they perform diverse locomotory patterns. In addition, the

ease of maintenance also makes this species a good choice for experimental fluid studies (Mwaffo et al. 2017). Zebra fish perform BCF locomotion and are further identified as carangiform swimmers (Yao et al. 2015). During carangiform swimming, the body undulations are confined to the last third of the body length, and thrust is provided by the caudal fin (Sfakiotakis et al. 1999).

The tested fish was an adult male zebra fish with a body length of $BL = 38$ mm. It was kept in an aquarium on a 12 h light/12 h dark lighting cycle and fed daily. The temperature was maintained at 26 ± 0.5 °C, and the acidity was maintained at pH= 7.2 (standard environment temperature and pH conditions for zebra fish). The water in the experimental water channel was kept under the same conditions during the experiment.

2.2 Tomographic PIV setup

The experiment was conducted in a recirculating open channel, with a dimension of 800 mm × 80 mm × 60 mm, located at the Institute of Fluid Engineering, Zhejiang University, China. As shown in Fig. 1, a swimming slot made by transparent acrylic plates was inserted into the water channel to reduce the free-swimming region. In other words, it decreased the time waiting for the tested fish to enter the testing region by setting a limited swimming space. With this additional constraint, the size of the measurement volume is 40 mm × 40 mm × 40 mm in x (streamwise), y (spanwise), and z (vertical) directions of the laboratory frame, respectively. And the tested fish was expected to swim along the slot against a water current. Similar constraints could be also found in Wolfgang et al. (1999a) and Mwaffo et al. (2017).

A 12 V DC micro-pump was installed at the right end of the swimming tunnel, which generated a 27 mm/s water current from right to left (along the positive x direction). To improve the freestream quality, honeycomb sections with three screens in each section were installed at the left and right ends of the tunnel. The water current velocity profiles of three components, measured upstream of the TPIV testing region, are shown in the inserted plot in Fig. 1. These velocity profiles were averaged from 18 statistically independent velocity field samples and plotted as functions of position along the z axis, which demonstrate a reasonably uniform flow across the measurement volume. No obvious velocity gradient near the edges of the measurement volume was observed. It is considered that the measurement volume did not overlap with the wall boundary layer. But, the maneuvers of the fish may cause blockage in the tunnel to some extent, and vortex image interactions potentially have influence on the behavior of the wake. This setup is designed to simulate a water current against which a zebra fish freely swims.

The tomographic particle image velocimetry tracers used were glass hollow particles with a diameter of approximately 50 μm and a density of 1.03 g/cm^3, which were uniformly spread in the recirculating water channel. The particle seeding density was approximately 0.05 particles per pixel. A dual-head ND:YLF laser (Vlite-Hi-527-50 from Beamtech Optronics Co., Ltd.) with an energy of 50 mJ per pulse and a repetition pulse rate of 500 Hz was equipped to illuminate the measurement volume. The wavelength of the laser was 527 nm. The laser beam was re-oriented and first collimated then expanded into a 40 mm thick light sheet by one concave lens and two convex lenses. The laser was emitted toward the zebra fish tail (from the left side of the swimming tunnel), and the illuminating orientation was parallel to the x axis, which could reduce the influence of fish body shadows. Four Photron FASTCAM cameras (two Photron FASTCAM SA4 cameras on the top and two Photron FASTCAM Mini AX100 cameras on the bottom) were fixed in an X-shaped arrangement from one side of the channel, as shown in Fig. 1. Each camera was equipped with a Nikon Micro Nikkor 200 mm focal-length macro-objective at $f_{\#} = 32$. The viewing angles between cameras and the light sheet were about 20°. The resolution of the cameras is 1024×1024, and the recording frequency of the TPIV system was 500 Hz. The cameras and high-frequency laser were synchronized and controlled by a Micropulse 725 Synchronizer from MicroVec., Inc.

The intensity-enhanced multiplicative algebraic reconstruction technique (IntE-MART) algorithm (Wang et al. 2016b) was used to reconstruct the three-dimensional particle field. To improve the quality of the mapping function, a self-calibration technique (Wieneke 2008) was employed. The TPIV calibration, data acquisition, and data processing were conducted on the MicroVec4 v1.2 (MicroVec., Inc.) software. Note that, the area of fish was cut out from the raw particle images before the 3D reconstruction process. The 3D reconstruct volume has a dimension of 25.4 mm × 37.5 mm × 22.5 mm. The magnification was 0.045 mm per voxel, resulting in a volume size of 620 × 906 × 562 voxels. The three-dimensional velocity fields
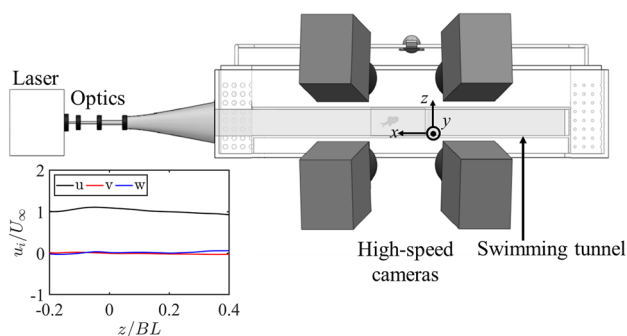

Fig. 1 Experimental setup and the coordinate system. Inset axes show the water current velocity profiles

were evaluated with the multi-pass correlation analysis with a deforming investigating window (Scarano 2001) of $32 \times 32 \times 32$ pixels. The initial interrogation volume was $48 \times 48 \times 48$ pixels and the final interrogation volume was $32 \times 32 \times 32$ pixels, resulting in a spatial resolution of 1.44 mm, approximately 3.6% of the fish body length. The resulting velocity vectors were distributed on a $74 \times 110 \times 67$ spatial grid corresponding to a physical domain of $[-11.1, 14.3] \times [-38.2, -0.7] \times [-8.3, 14.2]$ (mm). Note that, the physical location of the coordinate $[0, -20.0, 0]$ is at the center of the swimming tunnel.

To study the relation of the caudal fin and wake structures, SFM (Structure From Motion Schönberger and Frahm 2016) was used to reconstruct the caudal fin. Firstly, local features (i.e., gray distributions in the regions occupied by the caudal fin) were extracted from a image pair recorded by two cameras. Using a similarity metric, features in each image seeing the same scene were matched. Then, the sparse point cloud containing 3D coordinate information of the fin could be obtained by triangulation method. Note that, the image pair used for the caudal fin reconstruction was adopted from images recorded by two cameras of the TPIV system, and the same mapping function was used. Thus, a simultaneous recording of the wake and kinematic information of the caudal fin was achieved. To obtain a high quality reconstruction of the fin, the image pair should be properly chosen from the four TPIV images. Specifically, images taken by cameras which have a larger angle to the fishs heading direction are preferred. The images from the two right cameras are used for the reconstruction of the caudal fin in the current work.

2.3 Post-processing approaches and analysis methods

λ_{ci}-criterion, which is frame independent and excludes regions having vorticity but no local spiraling motion, was applied for an optimal visualization of flow structures. According to Zhou et al. (1999), the velocity gradient tensor $\nabla \boldsymbol{u}$ in Cartesian coordinates can be decomposed as

$$\nabla \boldsymbol{u} = \begin{bmatrix} \boldsymbol{v}_r & \boldsymbol{v}_{cr} & \boldsymbol{v}_{ci} \end{bmatrix} \begin{bmatrix} \lambda_r & 0 & 0 \\ 0 & \lambda_{cr} & \lambda_{ci} \\ 0 & \lambda_{ci} & \lambda_{cr} \end{bmatrix} \begin{bmatrix} \boldsymbol{v}_r & \boldsymbol{v}_{cr} & \boldsymbol{v}_{ci} \end{bmatrix}^{-1} \quad (1)$$

where λ_r is a real eigenvalue with a corresponding real eigenvector $\boldsymbol{v}_r$, and $\lambda_{cr} \pm \lambda_{ci} i$ are a pair of conjugate complex eigenvalues with corresponding eigenvectors $\boldsymbol{v}_{cr} \pm \boldsymbol{v}_{ci} i$. The local flow is either stretched or compressed along $\boldsymbol{v}_r$, depending on the sign of λ_r. In the plane spanned by $\boldsymbol{v}_{cr}$ and $\boldsymbol{v}_{ci}$, the local flow is swirling and the swirling strength is quantified by λ_{ci}. λ_{ci}-criterion can indicate the direction and strength of flow swirling and is widely used in the identification of a vortex. Note that, in some situations, the decomposition of $\nabla \boldsymbol{u}$ consists of three real eigenvalues with

three corresponding real eigenvectors. Under such circumstances, the calculated point is considered a repelling node, an attracting node, or even a saddle point, depending on the sign of eigenvalues (Chong et al. 1990; Ting and Yang 2009). Stretching or compressing dominates the local flow while no configuration of swirling is presented. In Sect. 3.2, this characteristic was used to detect critical point at the joint of the linked vortex rings (i.e., connecting part of adjacent vortex rings).

As a non-invasive technique based on the cross-correlation analysis of particle images, PIV measurement is inevitably subject to containing noise, outliers, and missing vectors in deduced velocity fields (Garcia 2011). These defects in velocity fields have a non-ignorable influence on calculating velocity derivatives, such as vorticity, λ_{ci} and other velocity gradient-based quantities. Thus, a robust divergence-free smoothing (DFS) algorithm (Wang et al. 2016a) was applied to the resulting velocity fields to remove data defects.

Figure 2 presents the comparison between original TPIV velocity data and DFS processed velocity data. The top left has isosurfaces of $\lambda_{ci} = 0.35\lambda_{ci,max}$ calculated from the original TPIV velocity data, which clearly exhibits the three-dimensional structure of the linked vortex rings in the wake of the caudal fin. The bottom left has the λ_{ci} isosurfaces calculated from DFS processed data. It is obvious that the DFS algorithm smooths and refines the λ_{ci} (as well as other velocity derivatives), while the main features of the flow structure have been well inherited. The velocity divergence error is greatly reduced by the DFS algorithm, according
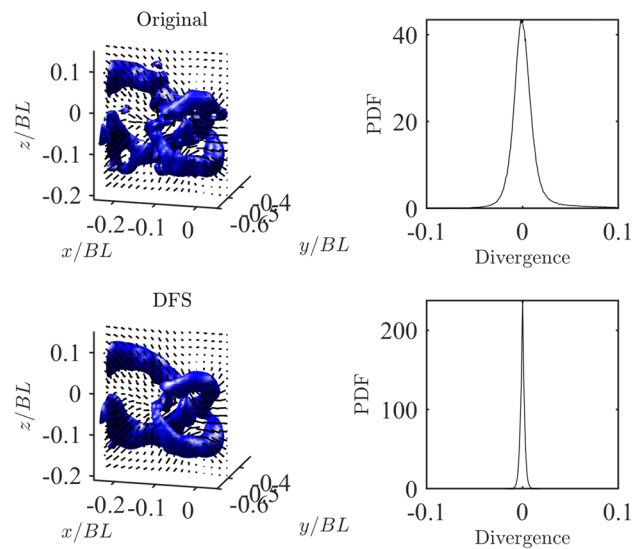

Fig. 2 The left column exhibits the isosurfaces of $\lambda_{ci} = 0.35\lambda_{ci,max}$ calculated from the original PIV velocity data (upper) and DFS processed velocity data (bottom). The right column shows the corresponding PDF of the velocity divergence errors

to the comparison of the corresponding probability density function (PDF) in the right column.

However, the DFS algorithm corrects TPIV data based on the divergence-free-constraint of the velocity field in one data frame. If the velocity data contain a series of frames, merely using DFS may not be sufficient to remove temporal defects in the data. To obtain an accurate calculation of acceleration, a pseudo-Lagrangian method (Wang et al. 2017) was applied. This approach uses multi-velocity fields to track imaginary particles. And it is operated iteratively until a convergence condition is satisfied. Then, an accurate acceleration can be derived from those refined imaginary particles velocities. For the reconstruction of pressure, a pressure correction scheme (PCS) for PIV data (PIV-PCS Wang et al. 2018) was applied, which could reduce the errors in the curl of the pressure gradient, and ensure that the flow field satisfies the dynamic constraints imposed by the incompressible Navier-Stokes equations. With a proper POD-based smoothing at the boundaries, the pressure can be directly solved from the velocity fields (Wang et al. 2018).

3 Results

As a principal nondimensional parameter, Strouhal number, $St = fA/U$ is used by researchers to describe the oscillatory propulsion pattern. Here, f is the pitching frequency, A is the wake width (commonly approximated by the caudal fin peak-to-peak amplitude), and U is the freestream velocity. This section exhibits a trial that the tested fish swam around 3.2 body length per second against the freestream ($Re = 4185 \pm 428$, $St = 0.48 \pm 0.05$). The relatively high pitching frequency $f = 8.3$ Hz, which is close to the observation from Mwaffo et al. (2017) under the same freestream velocity, leads to the estimated St being higher than the optimal range ($0.25 \leq St \leq 0.35$) of cruise presented by Triantafyllou et al. (1993). One hundred TPIV frames were recorded and processed to obtain a time-resolved three-dimensional dataset with a 0.2 sec duration. The time t of the first data frame is set to $t_0 = 0$ ms. A structure of linked vortex rings was clearly captured, and the corresponding velocity, acceleration and pressure fields were analyzed.

3.1 Structure of the linked vortex rings

Visualizing the wake together with the fin movement following the strategy of Mendelson and Techet (2015), Fig. 3 gives a brief three-dimensional description of the wake evolution in an interval of about half a pitching cycle. For a better visualization, the caudal fin is reconstructed and presented in the figure. The trajectories of the upper and lower tips of the caudal fin are presented as orange and red lines, respectively. Both trajectories are initiated since $t = 0$

ms. The tested fish heads approximately in the negative x direction, and its caudal fin sweeps along the y direction. The isosurfaces of $\lambda_{ci} = 0.35\lambda_{ci,max}$ (e.g., $\lambda_{ci,max} = 118$ s^{-1} at $t = 110$ ms) are shown to present vortex patterns in the wake. When $t = 82$ ms (Fig. 3a), a vortex ring (labeled as VR1) is already formed and shed from the caudal fin. Indicated by the fin tip trajectories, the caudal fin finishes the previous stroke and initiates the next stroke. Consistently, vortical structures are generated between VR1 and the caudal fin. As the fin continues to sweep, a C-shaped coherent structure is clearly seen at $t = 92$ ms (Fig. 3b), which is another vortex ring (labeled as VR2) that is not completely formed. When $t = 110$ ms (Fig. 3c), both VR1 and VR2 are completely formed and shed, and the structure of linked vortex rings is apparently presented. At $t = 122$ ms (Fig. 3d), VR1 maintains its coherence but partially deforms. It presents a tendency to cross through VR2, which may be caused by the induced velocity of VR2. At $t = 154$ ms (Fig. 3e), both vortex rings continuously deform. Note that, half of VR1 leaves the domain due to its downstream convection. Similar to the moment of $t = 92$ ms, vortical structures are observed around the caudal fin, which implies the generation of a new vortex ring in the wake. A short duration later (not provided in the figure), the structure of linked vortex rings is heavily dissipated. Hence, high unsteadiness is expected in the wake. According to Fig. 3, the pattern of linked vortex rings is clearly seen.

To further demonstrate the characteristics of the wake, Fig. 4a and b give a detailed three-dimensional description of the vortex structures at $t = 110$ ms, when VR2 is just shed from the caudal fin and the coherent structure of linked vortex rings is the clearest. Velocity vectors of u–w and contours of ω_y in the $y/BL = -0.51$ plane (around the spanwise midpoint of the measurement volume) are shown in Fig. 4a. The flow seems to converge upstream and present a high streamwise velocity through VR1, marked by the solid black arrow. The projection of VR1 on this plane is indicated by blue and yellow vorticity contours on the right, which exhibit strong rotations. Note that, this plane does not cut through VR2. As a result, no obvious vortical structure of VR2 is captured on the left of this cross section. Velocity vectors of u–v and contours of ω_z in the $z/BL = -0.05$ plane are shown in Fig. 4b. Jets J1 and J2 are marked with solid black arrows in the plane. A relatively high magnitude ω_z is marked by blue contours (negative) and yellow contours (positive), whose locations have a high agreement with the projection of λ_{ci} isosurfaces on this cross section. These contours visualize three in-plane vortices (V1, V2 and V3) with alternate in-plane rotating directions, which form the reverse von Kármán street (Triantafyllou et al. 1993). The wake exhibited a 2-S type pattern from a two-dimensional point of view, since three single vortices were observed downstream and no vortex pair could be seen (Williamson and Roshko
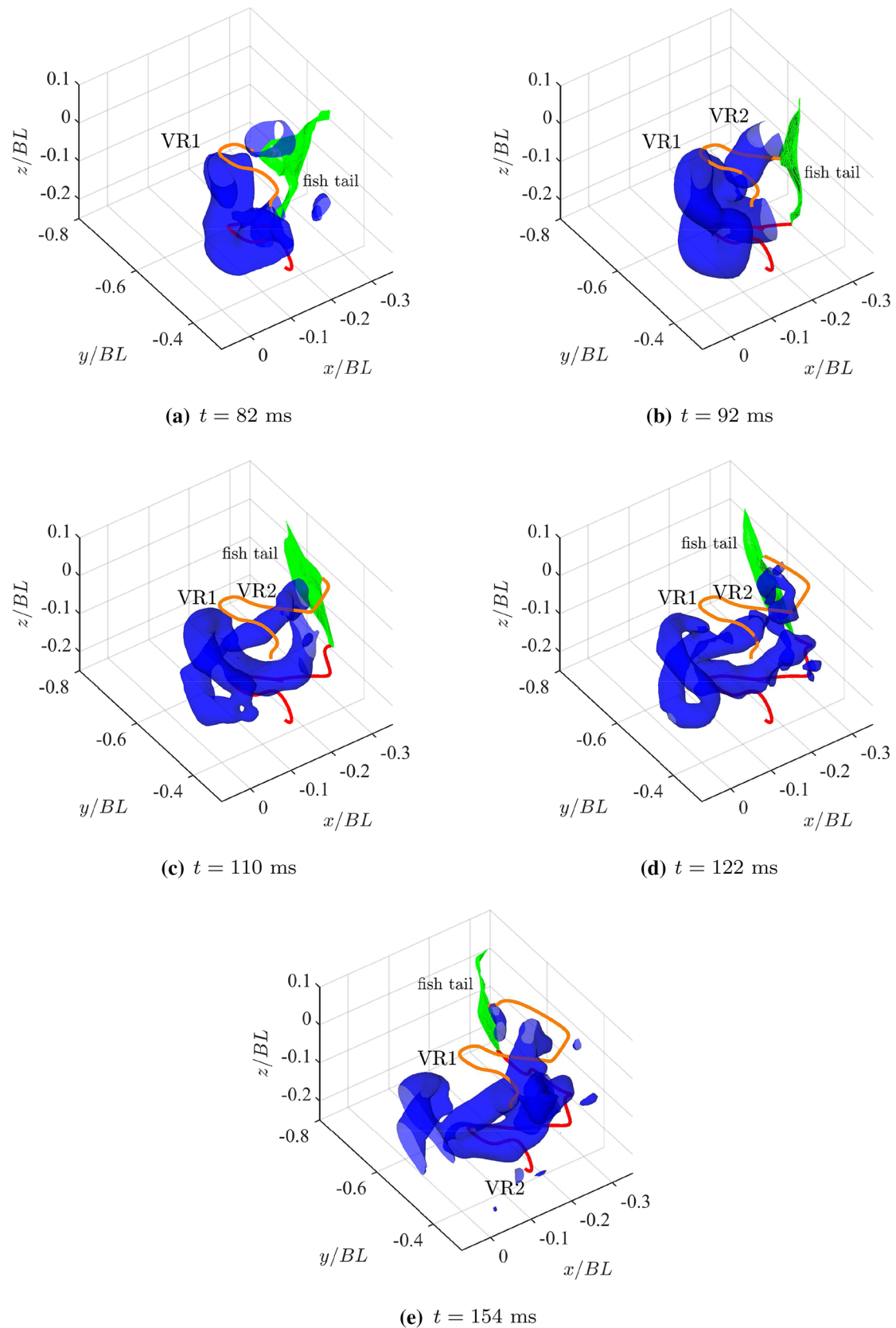
(a) $t = 82$ ms

(b) $t = 92$ ms

(c) $t = 110$ ms

(d) $t = 122$ ms

(e) $t = 154$ ms

Fig. 3 Isosurfaces of $\lambda_{ci} = 0.35\lambda_{ci,max}$ from $t = 82$ to 154 ms. The orange and red lines are the paths of the upper and lower caudal fin tips, respectively. The vortex ring closer to the caudal fin is labeled as VR2, and the downstream one is labeled as VR1
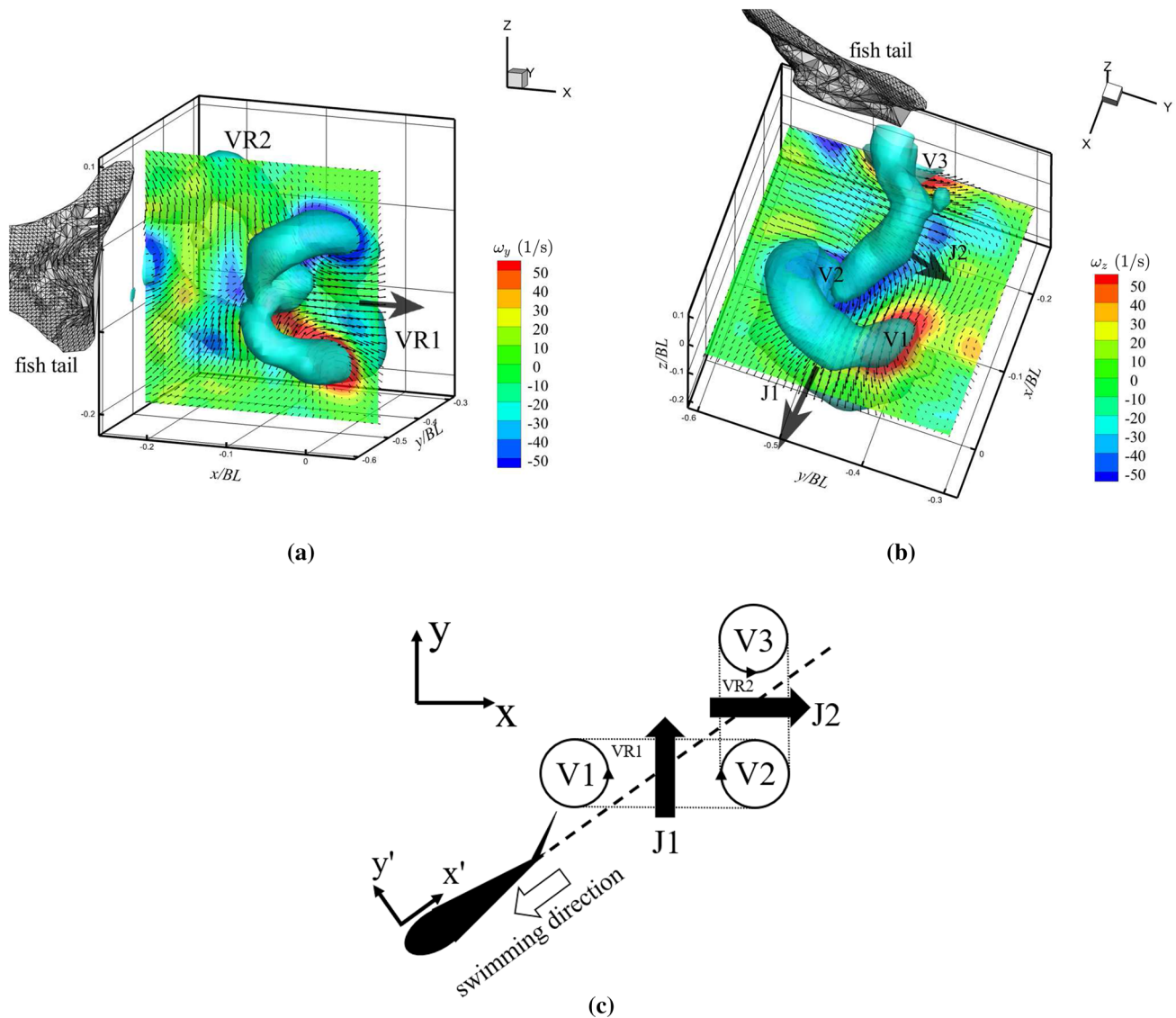
(a)

(b)

(c)

Fig. 4 The translucent isosurfaces of $\lambda_{ci} = 0.35\lambda_{ci,max}$ at $t = 110$ ms are displayed. Jets induced by vortex rings are labeled as J1 and J2. **a** shows ω_y superimposed with velocity components u–w in the $y/BL = -0.51$ plane; **b** shows vorticity component ω_z superimposed with velocity components u-v in the $z/BL = -0.05$ plane. In-plane vortices are labeled as V1, V2, and V3. **c** gives a corresponding schematic of swimming direction of the fish, vortices rotations and jets orientations

1988), and each vortex was shed per half pitching cycle. V1 and V3 are projections of VR1 and VR2, respectively. And V2 is the projection of the joint of the linked vortex rings on this cross section. Compared with the in-plane two-dimensional wake structures which may not give enough information for a correct interpretation of the wake (Flammang et al. 2011b), the three-dimensional flow visualization gives a more decent exhibition of the complicated structures of the linked vortex rings and presents the connection between each vortex in the street.

According to Fig. 4a and b, it is obvious that J1 and J2 have a small angle to the x axis and y axis, respectively. In other words, they are nearly perpendicular to each other. In

addition, the 3D wake structure has a high degree of horizontal symmetry. Meanwhile, it is noticed that swimming direction of the fish is not perfectly parallel to the x axis. By applying a fitting line on the averaged caudal fin trajectory (i.e., the average of the trajectories of the upper and lower tips), the swimming direction can be estimated, which is about 30° to the x axis and is almost parallel to the x–y plane. By anticlockwise rotating the original coordinates x–y along z by 30°, the new coordinate system x'–y'–z is obtained. Apparently, the x' axis is parallel to the swimming direction, while the y' axis is perpendicular to the swimming direction. Note that, the z axis is unchanged in the coordinate transformation. Then, the schematic in Fig. 4c can be drawn to

illustrate the wake structure from a top view and demonstrate the directions of fish swimming and the propulsive jets (J1 and J2). V1, V2 and V3, as well as their rotating directions, are marked as circles with arrows. Circles are connected by dotted lines to represent corresponding vortex rings. Jets J1 and J2 are marked as solid black arrows. And the swimming direction is presented as a black dash line. Detailed descriptions of the wake under the new coordinate system are given in supplementary information. Different from jets generated by man-made screw propellers, jets generated by the fish do not directly point posteriorly, i.e., downstream of the swimming direction (Drucker and Lauder 2002; Fish and Lauder 2006). Obviously, the components of the fish generated jets provide thrust momentum along the opposite swimming direction. At the same time, two opposite components of the jets, which have spatial distance along the swimming direction, generate a moment to balance the moment supporting the undulatory motions of fish swimming. The wake presents a zigzagging jet flow, which is similar to the observation of Wolfgang et al. (1999a) and Mwaffo et al. (2017). Therefore, the flow is periodically accelerated along the opposite swimming direction, which is a key phenomenon of a live fish swimming. The complicated flow pattern around critical point of the linked vortex rings will be further discussed in Sect. 3.2.

3.2 Acceleration and critical point

As mentioned in Sect. 2.3, a pseudo-tracing method is applied to calculate the total acceleration using material derivatives. Isosurfaces of acceleration components a'_x (parallel to the swimming direction) and a'_y (perpendicular to the swimming direction) are presented in Fig. 5a and b, respectively. The λ_{ci} isosurfaces (gray) are presented as a spatial reference.

The sizes of a'_y isosurfaces are larger than that of a'_x isosurfaces under the same threshold. In addition, the PDF of the acceleration components (see Fig. S2) suggests that the acceleration along the y' axis is comparable to and slightly stronger than the accelerating effect along the x' direction. This may hint that a strong acceleration component is needed in the direction perpendicular to the swimming direction during cruise. Namely, the positive a'_x is inferred to be corresponding to the force, which is against the resistance on the fish during the cruise. Hence, it could be relatively small if less energy is needed to maintain the optimal swimming strategy of the cruise. The a'_y component, on the contrary, reflects the relatively large variances along y' caused by VR2. Specifically, red a'_y isosurfaces indicate that the flow is accelerated to the positive y' direction in the upper and lower parts of VR2, which is consistent with the flow rotating direction at the same locations revealed by ω'_x in Fig. S1a. Negative a'_y (blue isosurface) at the joint of the linked vortex rings leads to the altering of the flow
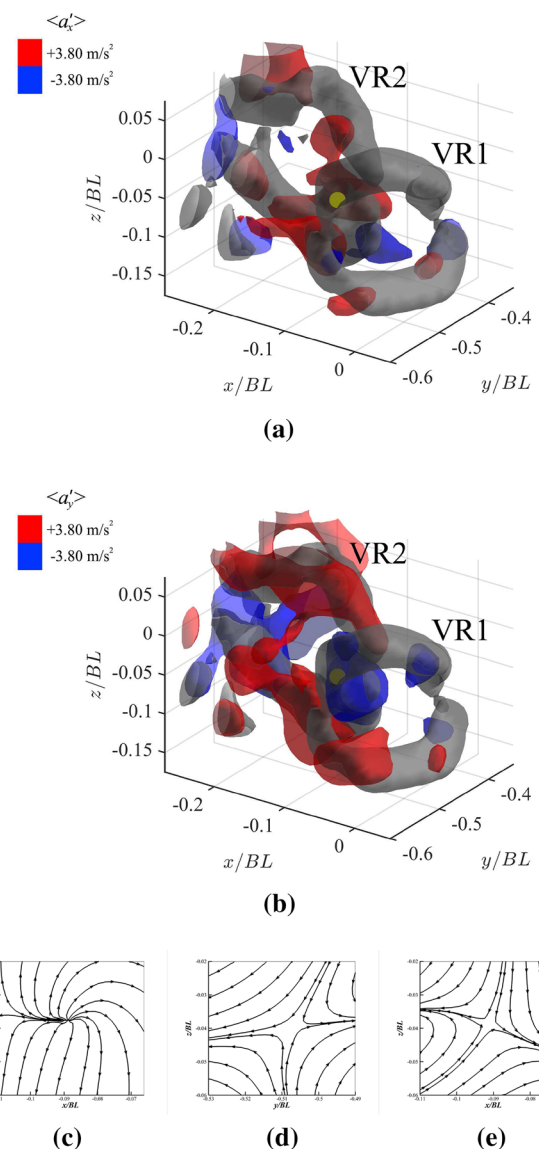

(a)

(b)

(c)   **(d)**   **(e)**

Fig. 5 Isosurfaces of a'_x and a'_y with isosurfaces of $\lambda_{ci} = 0.35\lambda_{ci,max}$ (gray) at $t = 110$ ms are given in (**a**) and (**b**), respectively. Critical points are marked as solid yellow dots. Streamlines around the critical point in x–y plane, y–z plane, and x–z plane are shown in (**c**–**e**), respectively

direction along the y' axis, which further results in the zigzagging jet flow shown in Fig. 4c. Note that, the caudal fin sweeps to the negative y' direction at $t = 110$ ms. Therefore, the blue a'_y isosurface near the caudal fin indicates the flow acceleration induced by the fin motion. The distribution of a'_y is relatively symmetrical up and down. The positive and negative a'_y in the wake combinedly cause a moment, which is believed to support the undulatory motions of the fish. This may explain why a'_y is stronger than a'_x around VR2, since that maintaining undulatory motion would be more energy consuming than overcoming the drag for the fish swimming. Similarly, computational investigation conducted by Bale et al. (2014) shows

that the fish spends most of the power to generate movement in the lateral direction (i.e., undulatory motions) and spends little power to move in the anteroposterior direction of swimming.

In addition, the accelerating effect is stronger around VR2 than that around VR1, which is indicated by the distributions of a_x' and a_y' isosurfaces. This highlights the wake evolution caused by the formation of VR2 and implies the generations of momentum and moment brought by the newly formed vortex ring. At the joint of the linked vortex rings, the alternation of the local velocity direction also plays an important role in the high acceleration. At the center of the joint, for example, $\partial v'/\partial t$ contributes a 38% portion of a_y', while the convective terms contribute the rest 62% of a_y'. This implies the direction change of J1 and J2, since the convective terms reveal the relatively large velocity gradient around the joint. Consequently, the local flow is greatly accelerated along y' not only because of the strong unsteadiness in the vicinity, but also for the sake of the velocity gradient around the joint. At the same location, $\partial u'/\partial t$ takes up a 95% portion of a_x', which is expected since the relatively uniform u' distribution at $t = 110$ ms (Fig. S1d) leads to small convective terms. As a result, the unsteady term should constitute the majority of a_x' at this location. In turn, this reveals the significance of resolved temporal information for the study of fish swimming.

It can be inferred from above discussion and Fig. 4c again that J1 and J2 have components opposite to the fish's heading direction. These components periodically launch in the wake in the form of a periodic jetting, serving as the major contributing factor of the forward motion of the fish and acting against the resistance during cruise. Meanwhile, J1 and J2 also have components perpendicular to the fish's heading direction, which results in a strong periodically varying moment acting on the fish. The resultant moment contributes to the body positioning during fish's undulatory swimming.

Another interesting phenomenon observed from Fig. 5 is that a topological critical point S exists approximately at the center of the joint ($x/BL = -0.09$, $y/BL = -0.51$, $z/BL = -0.04$, marked as a solid yellow dot in Fig. 5a and b). Around this critical point, there are strong $\partial v'/\partial x'$ (Fig. S1e) and strong $\partial w/\partial z$ (Fig. S1f), which suggests that the critical point is a typical 3D saddle point.

To quantitatively confirm the existence of this critical point, the velocity gradient tensor $\nabla \boldsymbol{u}$ at S is decomposed as

$$\nabla \boldsymbol{u} = \begin{bmatrix} \boldsymbol{v}_1 & \boldsymbol{v}_2 & \boldsymbol{v}_3 \end{bmatrix} \begin{bmatrix} \lambda_1 & 0 & 0 \\ 0 & \lambda_2 & 0 \\ 0 & 0 & \lambda_3 \end{bmatrix} \begin{bmatrix} \boldsymbol{v}_1 & \boldsymbol{v}_2 & \boldsymbol{v}_3 \end{bmatrix}^{-1} \tag{2}$$

which has a similar form to the λ_{ci} decomposition, but λ_i and $\boldsymbol{v}_i$ are all real eigenvalues and corresponding eigenvectors. As no complex eigenvalue is found, no local swirling behavior is expected, and only attracting/repelling motions can exist. To be specific, $\lambda_1 = -2.72$, $\lambda_2 = 0.93$, $\lambda_3 = 1.73$, and their corresponding eigenvectors are $\boldsymbol{v}_1 = (-0.36, -0.28, -0.89)$, $\boldsymbol{v}_2 = (0.72, -0.54, -0.44)$, $\boldsymbol{v}_3 = (-0.63, -0.76, 0.15)$. Apparently, the negative λ_1 results in an attracting effect along with $\boldsymbol{v}_1$. And repelling effects are expected along with $\boldsymbol{v}_2$ and $\boldsymbol{v}_3$, since that λ_2 and λ_3 are positive. Additionally, $\boldsymbol{v}_1$ and $\boldsymbol{v}_2$ have relatively small angles to the z axis and the x axis, respectively. Having three distinct real eigenvalues with one negative and two positives indicates that the critical point is of the *node/saddle/saddle* type. Figure 5c–e shows projections of velocity field on x–y, x–z and y–z planes. With local convection velocity removed, the local streamlines clearly indicate that the critical point is a node (source)/saddle/saddle type point. According to Chong et al. (1990), this point is *unstable* since P–Q–R and related derivatives at this point meet the classification criterion, where $P > 0$, $Q < 0$, and $0 < R < R_b$ ($R_b = \frac{1}{3}P(Q - \frac{2}{9}P^2) + \frac{2}{27}(-3Q + P^2)^{(3/2)}$). Similar decomposition was done by Ting and Yang (2009) in two-dimensional wakes generated by a live fish. Saddles were found near the repelling focuses, which represent vortices in the two-dimensional measuring plane. Ting and Yang (2009) also insisted that the flow near the saddle might be unstable, since the connection of a separatrix of a saddle point to a focus might form an unstable flow structure, from a topological perspective.

3.3 Reconstructed pressure distribution

Figure 6a shows isosurfaces of pressure and pressure contours in the $y/BL = -0.38$ and $z/BL = -0.04$ planes at $t = 110$ ms. Note that, the pressure solved by PIV-PCS is the relative pressure, and the reference pressure $p_0 = 0$ is set at one corner of the cubic data field (i.e., $x/BL = 0.32$, $y/BL = -0.07$, $z/BL = -0.17$).

Relatively high pressure regions are indicated by red isosurfaces near the caudal fin. It is inferred that the local high pressure distribution is created by the caudal fin pushing the fluid sideways away from it. Similarly, reconstructed two-dimensional pressure field around a cruising zebra fish from Mwaffo et al. (2017) exhibits high pressure regions near pitching caudal fins. Isosurfaces of relatively low pressure regions are presented further downstream. Numerical result from Wolfgang et al. (1999a) exhibits a similar pattern. Namely, relatively high pressure is generated around the caudal fin as it sweeps through the downstream low pressure region. One may notice that the C-shaped low pressure isosurfaces in Fig. 6a have a high agreement with the configuration of the linked vortex rings. It is predictable since flow with a relatively high velocity in vortex rings should create a relatively low pressure distribution. This pressure distribution leads to a net force which is beneficial to the fish locomotion, since regions with relatively higher pressure are located at upstream. Therefore, the jet in the wake is clearly revealed. It is further claimed that the flow separation from
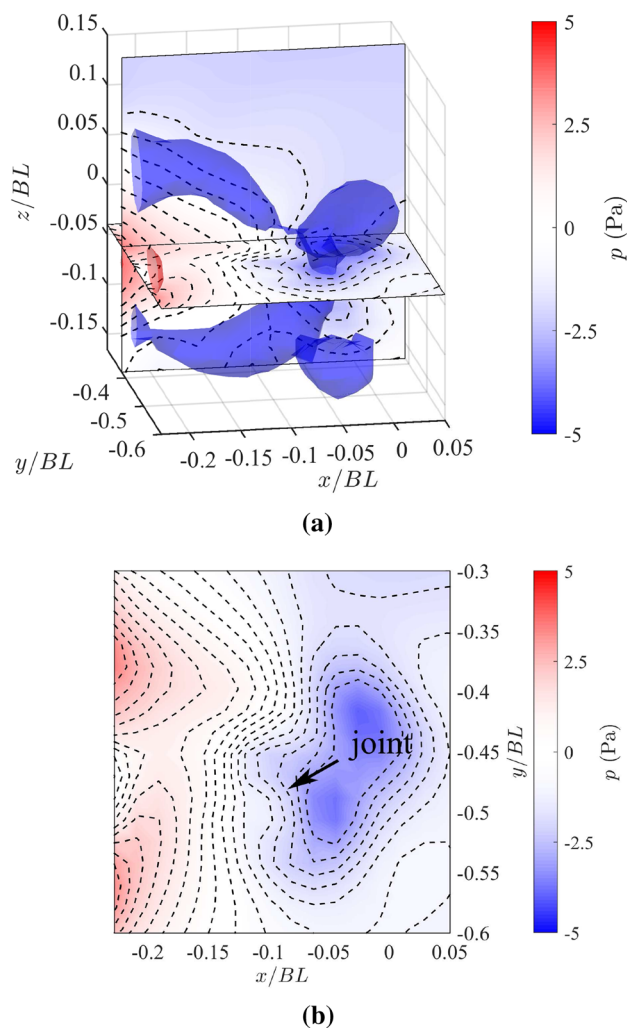
(a)

(b)

Fig. 6 **a** Isosurfaces of pressure (red: $p = +3.5$ Pa; blue: $p = -3.5$ Pa) superimposed with $y/BL = -0.38$ plane and $z/BL = -0.04$ plane at $t = 110$ ms. Pressure contours are marked with dotted lines in two inserted planes; **b** projection of reconstructed 3D pressure field on the $z/BL = -0.04$ plane

the fin contributes to the formation of a reverse von Kármán street (Wolfgang et al. 1999a). Indeed, the flow separation at the caudal fin tip introduces vorticity, and the local pressure gradient caused by the caudal fin's motion in the downstream low pressure region may also contribute to vorticity diffusing from the fin, which further feeds and strengths the downstream vortical structures.

Figure 6b shows the projection of the reconstructed 3D pressure field on the $z/BL = -0.04$ plane, which cuts through the high acceleration region at the joint mentioned in Sect. 3.2. A large pressure gradient is observed at the center of the field of view, which is indicated by dense dotted contour lines. This distribution is approximately consistent with the presence of high acceleration at the joint (Fig. 5b). Additionally, the relatively strong pressure gradient near the

caudal fin is consistent with the presence of upstream high acceleration regions shown in Fig. 5. It is reasonable since the acceleration is identical to the pressure gradient, if the viscous terms of the Navier-Stokes equations are ignored. Obviously, the pressure distribution has a strong correlation with the vortex patterns in the wake. And the characteristics of the pressure field agree well with the velocity and its derivative fields.

Further downstream of the joint of the linked vortex rings, the pressure gradient becomes smaller, which is again consistent with Fig. 5 that the acceleration effect weakens downstream of the joint. From a dynamics point of view, the joint of the linked vortex rings bears with a greater disturbance. As a result, the joint firstly breaks down at $t = 154$ ms (Fig. 3e), while the two vortex rings still could persist their C-shaped coherent structures.

4 Conclusions

The time-resolved three-dimensional measurement of wake structures generated by a live zebra fish has been carried out through the use of TPIV. The instantaneous structures behind the caudal fin have been clearly captured, as well as their temporal evolution.

The λ_{ci} isosurfaces, combined with contours of the vorticity components, demonstrate that the two vortex rings are linked with an angle. The shapes of isosurfaces and orientations of vortex rings are highly similar to previous phase-averaged observations (Imamura and Matsuuchi 2013). Different from man-made propellers, the linked vortex rings in the wake do not generate a continuous thrust momentum directly pointing downstream, but induce successive jets with periodic direction variation. These jets, considered as the reverse von Kármán street from a two-dimensional point of view, provide the momentum and moment for fish maneuvers. Specifically, the streamwise components of these jets contribute to the forward moving, while the spanwise components are expected to balance the moment of the undulatory motions. Indeed, the spanwise components of those jets play a role very similar to the "side jet" from Ting and Yang (2009) and multiple "side jets" for successive turns from Sakakibara et al. (2004). Therefore, one can speculate that by changing the orientations of vortex rings in the wake, fish can easily change the directions of their movements.

Acceleration of the wake is calculated, and the joint of the vortex rings is found to have a relatively high acceleration component perpendicular to the swimming direction. The analysis of the acceleration components hints that the undulatory motions consume a considerable part of the power during cruise. The critical point is analyzed by decomposing the velocity gradient tensor $\nabla \boldsymbol{u}$. The critical point classified in the P–Q–R space has a typical node/saddle/saddle

topology, which suggests that the wake near it is unstable. Since a saddle could be relevant to vortex shedding or vortex boundary, the critical point might be used to detect the shedding of vortices from the oscillating caudal fin and thus segment wakes by tailbeats. By looking at the unsteady terms in the high acceleration regions, high unsteadiness in the structure of linked vortex rings is revealed. The convective terms reveal the relatively large velocity gradient around the joint of the linked vortex rings, which again emphasizes the fact that the flow moving direction is altered through these vortex rings. Therefore, above facts show the importance of investigating live fish swimming in the aspect of 3D temporal evolution.

Pressure reconstruction has been applied to the time-resolved data, and low pressure regions are found around the linked vortex rings. The relatively high pressure distribution upstream further indicates that a net force parallel to the fish heading direction acts on the fish. As one can expect, a relatively large pressure gradient is observed around the joint of the linked vortex rings, due to the high acceleration at the same place. Since the critical point is also located at the joint, it is believed that pressure field would be more beneficial to the study of dynamics of fish swimming associated with flow stability in the future work.

In brief, the current work uses TPIV to record time-resolved data and then applies DFS, PIV-PCS and other methodologies to reconstruct three-dimensional wake structures and the corresponding pressure field. The results present high similarities to previous observations but further promote the understanding of the temporal evolution of these flow structures. In other bio-inspired experiments, TPIV measurement exhibits its ability and effectiveness in the reconstruction of wake structures of live fish. By properly installing the mirror, manipulating the image process and masking (e.g., visual hull method Adhikari and Longmire 2012), shadows and reflections caused by motions of the tested creature can be handled, and the near-body flow structures can be obtained.

References

Adhikari D, Longmire E (2012) Visual hull method for tomographic PIV measurement of flow around moving objects. Exp Fluids 53:943–964

Adhikari D, Longmire E (2013) Infrared tomographic PIV and 3D motion tracking system applied to aquatic predator-prey interaction. Meas Sci Technol 24:024011. https://doi.org/10.1088/0957-0233/24/2/024011

Adhikari D, Gemmell B, Hallberg M, Longmire E, Buskey E (2015a) Simultaneous measurement of 3D zooplankton trajectories and surrounding fluid velocity field in complex flows. J Exp Biol. https://doi.org/10.1242/jeb.121707

Adhikari D, Webster D, Yen J (2015b) Portable infrared tomographic PIV and 3D kinematics measurement of swimming sea butterfly. In: 11th International Symposium on Particle Image Velocimetry. https://doi.org/10.13140/RG.2.1.2265.1362

Adhikari D, Webster D, Yen J (2016) Portable tomographic PIV measurements of swimming shelled Antarctic pteropods. Exp Fluids. https://doi.org/10.1007/s00348-016-2269-7

Bale R, Hao M, Bhalla A, Patankar N (2014) Energy efficiency and allometry of movement of swimming and flying animals. Proc Natl Acad Sci 111:7517–7521. https://doi.org/10.1073/pnas.1310544111

Borazjani I, Sotiropoulos F (2008) Numerical investigation of the hydrodynamics of carangiform swimming in the transitional and inertial flow regimes. J Exp Biol 211:1541–58. https://doi.org/10.1242/jeb.015644

Breder C (2015) Locomotion of fishes. Zoologica 4:159–291

Brooks S, Green M (2019) Experimental study of body-fin interaction and vortex dynamics generated by a two degree-of-freedom fish model. Biomimetics 4:67. https://doi.org/10.3390/biomimetics4040067

Chong M, Perry A, Cantwell B (1990) A general classification of three-dimensional flow fields. Phys Fluids A: Fluid Dyn 2:765–777. https://doi.org/10.1063/1.857730

Danos N, Lauder G (2007) The ontogeny of fin function during routine turns in zebrafish danio rerio. J Exp Biol 210:3374–86. https://doi.org/10.1242/jeb.007484

Drucker E, Lauder G (2002) Experimental hydrodynamics of fish locomotion: functional insights from wake visualization. Integr Comp Biol 42:243–57. https://doi.org/10.1093/icb/42.2.243

Elsinga G, Scarano F, Wieneke B, Oudheusden B (2006) Tomographic particle image velocimetry. Exp Fluids 41:933–947. https://doi.org/10.1007/s00348-006-0212-z

Fish F, Lauder G (2006) Passive and active flow control by swimming fishes and mammals. Annu Rev Fluid Mech 38:193–224. https://doi.org/10.1146/annurev.fluid.38.050304.092201

Flammang B, Lauder G, Troolin D, Strand T (2011) Volumetric imaging of fish locomotion. Biol Let 7:695–8. https://doi.org/10.1098/rsbl.2011.0282

Flammang B, Lauder G, Troolin D, Strand T (2011) Volumetric imaging of shark tail hydrodynamics reveals a three-dimensional dual-ring vortex wake structure. Proc Biol Sci/R Soc 278:3670–8. https://doi.org/10.1098/rspb.2011.0489

Fujisawa N, Tanahashi S, Karkenahalli S (2005) Evaluation of pressure field and fluid forces on a circular cylinder with and without rotational oscillation using velocity data from PIV measurement. Meas Sci Technol 16:989. https://doi.org/10.1088/0957-0233/16/4/011

Gao Q, Wang H, Shen G (2013) Review on development of volumetric particle image velocimetry. Chin Sci Bull 58:4541–4556. https://doi.org/10.1007/s11434-013-6081-y

Garcia D (2011) A fast all-in-one method for automated post-processing of PIV data. Exp Fluids 50:1247–1259. https://doi.org/10.1007/s00348-010-0985-y

Gemmell B, Adhikari D, Longmire E (2014) Volumetric quantification of fluid flow reveals fish's use of hydrodynamic stealth to capture evasive prey. J R Soc Interface/R Soc 11:20130880. https://doi.org/10.1098/rsif.2013.0880

Green M, Rowley C, Smits A (2011) The unsteady three-dimensional wake produced by a trapezoidal pitching panel. J Fluid Mech 685:117–145. https://doi.org/10.1017/jfm.2011.286

Hale M (2002) S- and C-start escape responses of the muskellunge (Esox masquinongy) require alternative neuromotor mechanisms. J Exp Biol 205:2005–16

Huhn F, Schanz D, Gesemann S, Schröder A (2016) FFT integration of instantaneous 3D pressure gradient fields measured by Lagrangian particle tracking in turbulent flows. Exp Fluids 57:1–11. https://doi.org/10.1007/s00348-016-2236-3

Imamura N, Matsuuchi K (2013) Relationship between vortex ring in tail fin wake and propulsive force. Exp Fluids 54:1–13. https://doi.org/10.1007/s00348-013-1605-4

Kat R, Humble R, Oudheusden B (2010) Time-resolved PIV study of a transitional shear-layer around a square cylinder. In: IUTAM Symposium on Bluff Body Wakes and Vortex-Induced Vibrations (BBVIV-6), pp 265–268

King J, Kumar R, Green M (2018) Experimental observations of the three-dimensional wake structures and dynamics generated by a rigid, bioinspired pitching panel. Phys Rev Fluids. https://doi.org/10.1103/PhysRevFluids.3.034701

Küchemann D (1965) Report on the IUTAM symposium on concentrated vortex motions in fluids. J Fluid Mech 21(1):1–20

Lighthill M (1969) Hydromechanics of aquatic animal propulsion. Annu Rev Fluid Mech 1:413–446

Mendelson L, Techet A (2015) Quantitative wake analysis of a freely swimming fish using 3D synthetic aperture PIV. Exp Fluids 56:1–19. https://doi.org/10.1007/s00348-015-2003-x

Mendelson L, Techet A (2017) Multi-camera volumetric PIV for the study of jumping fish. Exp Fluids 59:10. https://doi.org/10.1007/s00348-017-2468-x

Mendelson L, Techet A (2020) Jumping archer fish exhibit multiple modes of fin-fin interaction. Bioinspiration Biomimet 16:016006. https://doi.org/10.1088/1748-3190/abb78e

Michaelis D (2014) Time resolved volumetric visualization of zooplankton body and surrounding flow field using advanced masking in tomographic PIV. 16th Int Symp on Flow Visualization. Okinawa, Japan

Mignano Anthony P, Kadapa Shraman, Tangorra James L, Lauder George V (2019) Passing the wake: using multiple fins to shape forces for swimming. Biomimetics 4:23

Mohaghar M, Adhikari D, Webster DR (2019) Characteristics of swimming shelled Antarctic pteropods (Limacina helicina antarctica) at intermediate Reynolds number regime. Phys Rev Fluids 4(11):111101

Murphy D, Webster D, Yen J (2012) A high-speed tomographic PIV system for measuring zooplanktonic flow. Limnol Oceanogr Methods 10:1096–1112. https://doi.org/10.4319/lom.2012.10.1096

Murphy D, Webster D, Yen J (2013) The hydrodynamics of hovering in Antarctic krill. Limnol Oceanogr: Fluids Environ 3:240–255. https://doi.org/10.1215/21573689-2401713

Murphy D, Adhikari D, Webster D, Yen J (2016) Underwater flight by the planktonic sea butterfly. J Exp Biol 219:535. https://doi.org/10.1242/jeb.129205

Mwaffo V, Zhang P, Cruz S, Porfiri M (2017) Zebrafish swimming in the flow: a particle image velocimetry study. PeerJ 5:e4041. https://doi.org/10.7717/peerj.4041

Oudheusden B (2013) PIV-based pressure measurement. Meas Sci Technol 24:032001. https://doi.org/10.1088/0957-0233/24/3/032001

Sakakibara J, Nakagawa M, Yoshida M (2004) Stereo-PIV study of flow around a maneuvering fish. Exp Fluids 36:282–293. https://doi.org/10.1007/s00348-003-0720-z

Scarano F (2001) Iterative image deformation methods in PIV. Meas Sci Technol 13:R1. https://doi.org/10.1088/0957-0233/13/1/201

Scarano F (2012) Tomographic PIV: principles and practice. Meas Sci Technol 24:012001. https://doi.org/10.1088/0957-0233/24/1/012001

Schönberger J, Frahm JM (2016) Structure-from-motion revisited. In: Proceedings of the IEEE conference on computer vision and pattern recognition, pp 4104–4113. https://doi.org/10.1109/CVPR.2016.445

Sfakiotakis M, Lane D, Davies J (1999) Review of fish swimming modes for aquatic locomotion. IEEE J Ocean Eng 24:237–252. https://doi.org/10.1109/48.757275

Shih A, Mendelson L, Techet A (2017) Archer fish jumping prey capture: kinematics and hydrodynamics. J Exp Biol 220:1411–1422. https://doi.org/10.1242/jeb.145623

Skipper A, Murphy D, Webster D (2019) Characterization of hop-and-sink daphniid locomotion. J Plankton Res 41:142–153. https://doi.org/10.1093/plankt/fbz003

Ting SC, Yang JT (2009) Extracting energetically dominant flow features in a complicated fish wake using singular-value decomposition. Phys Fluids 21:041901. https://doi.org/10.1063/1.3122802

Triantafyllou G, Triantafyllou M, Grosenbaugh M (1993) Optimal thrust development in oscillating foils with application to fish propulsion. J Fluids Struct 7:205–224. https://doi.org/10.1006/jfls.1993.1012

Triantafyllou M, Triantafyllou G, Yue D (2000) Hydrodynamics of fish-like swimming. ARFM 32:33–53

Tytell E, Lauder G (2008) Hydrodynamics of the escape response in bluegill sunfish, lepomis macrochirus. J Exp Biol 211:3359–69. https://doi.org/10.1242/jeb.020917

Wang C, Gao Q, Wang H, Runjie W, Li T, Wang J (2016) Divergence-free smoothing for volumetric PIV data. Exp Fluids 57:15. https://doi.org/10.1007/s00348-015-2097-1

Wang C, Gao Q, Wang J, Wang B, Pan C (2019) Experimental study on dominant vortex structures in near-wall region of turbulent boundary layer based on tomographic particle image velocimetry. J Fluid Mech 874:426–454. https://doi.org/10.1017/jfm.2019.412

Wang H, Gao Q, Runjie W, Wang J (2016) Intensity-enhanced MART for tomographic PIV. Exp Fluids 57:87. https://doi.org/10.1007/s00348-016-2176-y

Wang H, Gao Q, Wang Z, Wang J (2018) Error reduction for time-resolved PIV data based on Navier-Stokes equations. Exp Fluids 59:149. https://doi.org/10.1007/s00348-018-2605-1

Wang Z, Gao Q, Pan C, Feng L, Wang J (2017) Imaginary particle tracking accelerometry based on time-resolved velocity fields. Exp Fluids 58(9):113

Wieneke B (2008) Volume self-calibration for 3D particle image velocimetry. Exp Fluids 45:549–556. https://doi.org/10.1007/s00348-008-0521-5

Williamson C, Roshko A (1988) Vortex formation in the wake of an oscillating cylinder. J Fluid Struct 2:355–381. https://doi.org/10.1016/S0889-9746(88)90058-8

Witt W, Wen L, Lauder G (2015) Hydrodynamics of C-start escape responses of fish as studied with simple physical models. Integr Comp Biol 55:728–739. https://doi.org/10.1093/icb/icv016

Wolfgang M, Anderson J, Grosenbaugh M, Yue D, Triantafyllou M (1999) Near-body flow dynamics in swimming fish. J Exp Biol 202(Pt 17):2303–27

Wolfgang M, Triantafyllou M, Yue D (1999) Visualization of complex near-body transport processes in flexible-body propulsion. J Vis 2:143–151. https://doi.org/10.1007/BF03181517

Yao W, Lv Y, Gong X, Wu J, Bao B (2015) Different ossification patterns of intermuscular bones in fish with different swimming modes. Biol Open 4:1727–1732. https://doi.org/10.1242/bio.012856

Zhou J, Adrian R, Balachandar S, Kendall T (1999) Mechanisms for generating coherent packets of hairpin vortices in channel flow. J Fluid Mech 387:353–396. https://doi.org/10.1017/S002211209900467X

Zhu H, Wang C, Wang H, Wang J (2017) Tomographic PIV investigation on 3D wake structures for flow over a wall-mounted short cylinder. J Fluid Mech 831:743–778. https://doi.org/10.1017/jfm.2017.647

Zhu Q, Yue D (2002) Three-dimensional flow structures and vorticity control in fish-like swimming. J Fluid Mech 468:1–28. https://doi.org/10.1017/S002211200200143X